



OPEN

Oxidative coupling of methane—comparisons of $\text{MnTiO}_3\text{--Na}_2\text{WO}_4$ and $\text{MnO}_x\text{--TiO}_2\text{--Na}_2\text{WO}_4$ catalysts on different silica supports

Worapinit Tiyatha^{1,2}, Thanaphat Chukeaw^{1,2}, Sarannuch Sringam^{1,2}, Thongthai Witoon^{1,2,3}, Metta Chareonpanich^{1,2,3}, Günther Rupprechter⁴ & Anusorn Seubsai^{1,2,3}✉

The oxidative coupling of methane (OCM) converts CH_4 to value-added chemicals (C_{2+}), such as olefins and paraffin. For a series of $\text{MnTiO}_3\text{--Na}_2\text{WO}_4$ ($\text{MnTiO}_3\text{--NW}$) and $\text{MnO}_x\text{--TiO}_2\text{--Na}_2\text{WO}_4$ (Mn-Ti-NW), the effect of loading of MnTiO_3 or $\text{MnO}_x\text{--TiO}_2$, respectively, on two different supports (sol-gel SiO_2 (SG) and commercial fumed SiO_2 (CS)) was examined. The catalyst with the highest C_{2+} yield (21.6% with 60.8% C_{2+} selectivity and 35.6% CH_4 conversion) was 10 wt% $\text{MnTiO}_3\text{--NW/SG}$ with an olefins/paraffin ratio of 2.2. The catalyst surfaces with low oxygen-binding energies were associated with high CH_4 conversion. Stability tests conducted for over 24 h revealed that SG-supported catalysts were more durable than those on CS because the active phase (especially Na_2WO_4) was more stable in SG than in CS. With the use of SG, the activity of $\text{MnTiO}_3\text{--NW}$ was not substantially different from that of Mn-Ti-NW , especially at high metal loading.

Methane (CH_4) is a major chemical feedstock with a tetrahedral structure. The primary chemical conversions of CH_4 include oxidation, syngas reforming, and halogenation¹, which are difficult to control. The lifetime of CH_4 in the environment is much shorter than that of CO_2 , but CH_4 traps radiation more efficiently than CO_2 . Therefore, CH_4 has a greater impact on global warming than the same amount of CO_2 ². Indeed, the cumulative influence of CH_4 over 100 years is estimated to be 25 times greater than that of CO_2 ³. In recent years, the total CH_4 emissions have been found to result from natural gas and petroleum systems (30%), enteric fermentation (27%), landfills (17%), manure management (9%), and coal mining (7%), and others (10%)³. Processes for an efficient conversion of CH_4 to useful chemicals are, therefore, of great interest to reduce the amount of CH_4 released to the atmosphere.

Methane can be used both *indirectly* and *directly* to produce high-value hydrocarbons, such as olefins and paraffin = C_{2+} . The indirect methods use methane steam reforming, dry reforming, or partial oxidation as the first process for the production of synthesis gas (CO and H_2). Subsequently, Fischer–Tropsch and methanol synthesis processes are applied to generate value-added products⁴. The indirect methods are currently commercially applied in the petrochemical industry⁵, but direct methods would be clearly beneficial.

A feasible route is the direct conversion of methane to C_{2+} via oxidative coupling of methane (OCM) either by heterogeneous catalytic or homogeneous non-catalytic processes. The OCM reaction occurs at high temperatures (700–900 °C) at atmospheric pressure and requires only oxygen as the co-reactant in an inert gas (such as nitrogen) feed. As the non-catalytic process suffers from low methane conversion and selectivity, a heterogeneous catalytic process is desirable. Therefore, having a suitable solid catalyst is a prerequisite for the catalytic OCM process before commercialization to become industrially viable.

The OCM reaction is capable of generating C_{2+} , specifically ethylene (C_2H_4), but yields below 20% prevent commercial OCM. Under appropriate process conditions, yields of 30% have been reported in laboratory tests,

¹Department of Chemical Engineering, Faculty of Engineering, Kasetsart University, Bangkok 10900, Thailand. ²Center of Excellence on Petrochemical and Materials Technology, Kasetsart University, Bangkok 10900, Thailand. ³Research Network of NANOTEC–KU on NanoCatalysts and NanoMaterials for Sustainable Energy and Environment, Kasetsart University, Bangkok 10900, Thailand. ⁴Institute of Materials Chemistry, TU Wien, 1060 Vienna, Austria. ✉email: fengasn@ku.ac.th

with a minimum C_2H_4 yield of 25% required to make the method economically feasible (35–50% would be more practical)⁶. Generally, to be commercially attractive, C_{2+} selectivity and CH_4 conversion in OCM must exceed 80% and 30%, respectively⁷, which has stimulated research for many years⁸. However, despite exhaustive efforts, the OCM reaction still lacks a highly active and stable catalyst with high performance for C_{2+} formation.

Previous studies have indicated that Na_2WO_4 - MnO_x - SiO_2 -based catalysts were among the most active ones that yielded high C_{2+} selectivity at high CH_4 conversions, resulting in a C_{2+} yield of 10–35%^{9–19}. The high performance of these catalysts resulted from a complex combination of several factors, as inferred from literature. Some interesting facts on the active components are detailed as follows:

- i. Na atoms are necessary for the phase transition of amorphous SiO_2 to crystalline α -cristobalite at low calcination temperature (800 °C)^{20,21}. It is noteworthy that the usual temperature for this phase change is approximately 1500 °C²². Additionally, the mobility of Na^+ species during OCM at high temperatures (750–850 °C) can create active sites on the catalyst surface, facilitating hydrogen abstraction of CH_4 ²³. Moreover, it was suggested that Na^+ aids in the stability of the active WO_4 phase²⁴. Furthermore, it was claimed that active Na_2O species can be generated in small amounts in the catalytically relevant temperature regime (above 600 °C), and these Na_2O species are responsible for high activity and C_{2+} selectivity²⁵.
- ii. In a study of Na_2WO_4/SiO_2 using temporal analysis of products (TAP) and steady-state OCM reaction studies, the Na- WO_x sites on the surface were indicated to be responsible for the selective activation of CH_4 to C_2H_x and over-oxidation of CH_y to CO. On the other hand, the molten Na_2WO_4 phase promotes the oxidative dehydrogenation of C_2H_6 to C_2H_4 , but it is also responsible for the over-oxidation of CH_4 to CO_2 ²⁶.
- iii. WO_4 and MnO_x are the crucial active components for the generation of C_{2+} products. They cooperate during the reaction as follows. Initially, the O^{2-} species associated with the surface WO_4 (W^{6+}) sites, especially the tetrahedral form²⁷, activates CH_4 into a gaseous methyl radical. As a result, the W^{6+} center is transformed to W^{5+} with one chemical bond of $W-OH$. Thereafter, the oxidation of W^{5+} to W^{6+} occurs through electron transfer from W^{5+} to Mn^{3+} , subsequently reducing Mn^{3+} to Mn^{2+} . Finally, the oxidation of Mn^{2+} to Mn^{3+} occurs via reaction with gaseous oxygen, which generates an OH radical and an active oxygen atom^{28–30}. In other words, the MnO_x species boosts the oxygen mobility in the catalyst, resulting in an improved exchange of gaseous and surface oxygen³¹. Additionally, an in-depth study of Mn addition to $5Na_2WO_4/SiO_2$ catalyst revealed that Mn enhances the formation of both dissolved O_2 and lattice atomic O species, which are responsible for catalyzing the OCM reaction. Therefore, the CH_4 conversion toward C_{2+} formation is improved^{32,33}.
- iv. The addition of TiO_2 into the MnO_x - Na_2WO_4/SiO_2 catalyst further reduces the temperature of CH_4 activation in the OCM reaction to approximately 650–720 °C. This is probably due to the formation of a $MnTiO_3$ phase that enables the transition of Mn^{2+} to Mn^{3+} at a lower temperature than that of the MnO_x phase³⁴.
- v. The α -cristobalite SiO_2 is considered to assist CH_4 activation (although the underlying mechanism is unclear)^{15,20}, but upon calcination (starting with amorphous SiO_2), the surface area of the support declines substantially^{14,35}. Accordingly, some reports have shown that the phase transformation during the reaction causes catalyst deactivation^{27,36}. Other causes for catalyst deactivation may include the decomposition of active phases (such as Na_2WO_4)^{37–39} and/or loss of Na_2O due to sublimation during the reaction²⁵.

In several other studies, catalysts containing Mn, Na, Ti, W, and/or mesoporous SiO_2 have been claimed as highly active for OCM^{27,29,34,38–42} with $MnTiO_3$, MnO_x , and TiO_2 components being recommended as critical active phases for CH_4 activation. Many studies have attempted to further improve the C_{2+} selectivity and CH_4 conversion of Na_2WO_4 - MnO_x - SiO_2 -based catalysts by understanding the mechanism over the surface. For example, a study on the addition of H_2O to the testing system revealed that H_2O did not change the overall scheme of product formation but it was able to reduce the contribution of direct oxidation of CH_4 to CO_2 ⁴³. The effect of pressure was studied on the performance of $Mn/Na_2WO_4/SiO_2$, which revealed that the increase of pressure leads to higher C_{2+} selectivity and can accelerate unselective gas-phase reactions more than surface catalyzed processes¹⁹. It is also possible that the CH_4 conversions of 60–75% range could be obtained at a maximized C_{2+} yield in each specific reactor setup¹⁹. Our previous investigation of $MnTiO_3$ and Na_2WO_4 on different silica-based supports (fumed SiO_2 , MCM-41, and SBA-15) showed that the presence of $MnTiO_3$ and Na_2WO_4 on SBA-15 substantially increased CH_4 activation of CH_3 and H radicals, causing the OCM reaction to efficiently generate C_{2+} hydrocarbons²⁷. However, the $MnTiO_3$ nanocomposite has been less studied than the $MnO_x + TiO_2$ nanocomposite. Furthermore, the preparation of sol-gel SiO_2 has never been combined with such catalysts. We have speculated that a catalyst prepared using the sol-gel SiO_2 may resist catalyst deactivation better when fumed SiO_2 is used. Therefore, the current study aimed for a systematic comparison of the activity/selectivity of $MnTiO_3$ - Na_2WO_4 and MnO_x - TiO_2 - Na_2WO_4 supported on different silica-based supports (sol-gel SiO_2 and commercial fumed SiO_2). The results should reveal: (i) Whether the $MnTiO_3$ phase indeed functions better in the OCM reaction than the nanocomposite mixture of MnO_x and TiO_2 , and (ii) Whether the type of SiO_2 support has a substantial influence on catalytic performance.

Results and discussion

Activity of catalysts in the OCM reaction. The nanocomposite $MnTiO_3$ -NW/CS, $MnTiO_3$ -NW/SG, and Mn-Ti-NW/SG catalysts, containing 0–20 wt% of $MnTiO_3$ or Mn-Ti, respectively, were tested for the OCM reaction (Table 1, Supplementary Figure S1). Considering the catalyst performance in terms of C_{2+} yield per catalyst mass, when the amount of $MnTiO_3$ or Mn-Ti increased from 0 to 5 or 10 wt%, respectively, the corresponding activities suddenly increased, but then maintained the maximum values for higher loadings. The high-

Catalyst	Olefins selectivity (%)	Paraffins selectivity (%)	Olefins/paraffins (mol/mol)	C ₂₊ selectivity (%)	CH ₄ conversion (%)	C ₂₊ yield (%)	r _{C₂₊} [*]
NW/CS	18.2	13.7	1.3	33.1	21.9	7.2	0.42
5MnTiO ₃ -NW/CS	37.2	17.6	2.1	58.1	35.5	20.6	0.60
10MnTiO ₃ -NW/CS	37.6	17.0	2.2	57.8	35.7	20.6	0.40
15MnTiO ₃ -NW/CS	34.2	17.5	2.0	54.7	34.4	18.8	0.28
20MnTiO ₃ -NW/CS	27.6	15.2	1.8	45.0	31.7	14.4	0.17
NW/SG	14.5	12.1	1.2	27.5	20.5	5.6	0.33
5MnTiO ₃ -NW/SG	32.2	18.8	1.7	53.8	29.9	16.2	0.47
10MnTiO ₃ -NW/SG	39.1	18.1	2.2	60.8	35.6	21.6	0.42
15MnTiO ₃ -NW/SG	39.0	18.0	2.2	60.5	35.5	21.4	0.31
20MnTiO ₃ -NW/SG	39.6	18.1	2.2	61.3	35.3	21.6	0.25
5Mn-Ti-NW/SG	38.5	17.0	2.3	59.0	35.4	20.9	0.60
10Mn-Ti-NW/SG	37.9	17.1	2.2	58.5	35.4	20.7	0.40
15Mn-Ti-NW/SG	38.3	17.6	2.2	59.3	35.0	20.8	0.30
20Mn-Ti-NW/SG	39.4	17.5	2.3	60.5	35.5	21.5	0.24

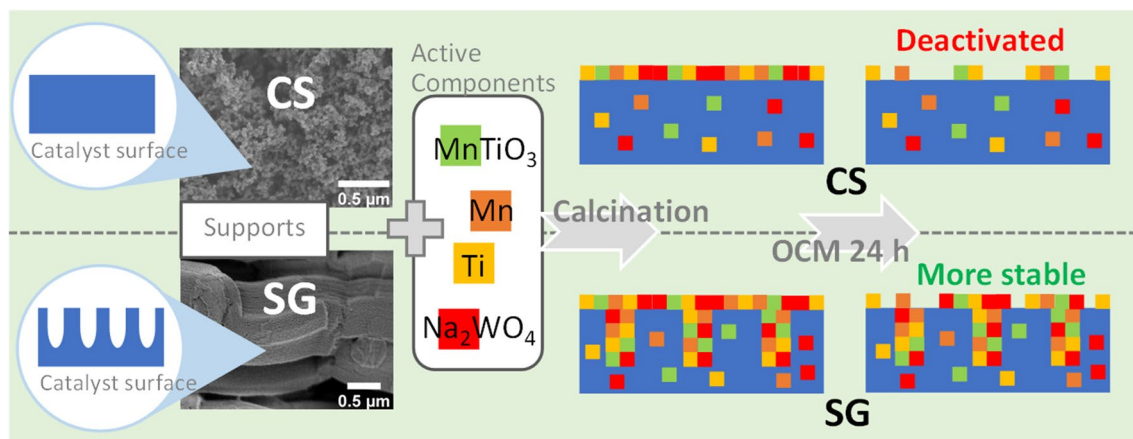
Table 1. Performance of OCM catalysts. Testing conditions: 50 mg catalyst, gas feed of CH₄:O₂:N₂ = 3:1:4, reactor temperature = 700 °C, atmospheric pressure, total gas flow rate = 50 mL min⁻¹ (GHSV = 30,588 h⁻¹). *r_{C₂₊} = moles of C₂₊/[(total moles of MnTiO₃ or (Mn + Ti) and Na₂WO₄) × h].

est C₂₊ yields achieved were 20.6% (58.0% C₂₊ selectivity with 35.5% CH₄ conversion) for 5 wt% MnTiO₃-NW/CS, 21.6% (60.8% C₂₊ selectivity with 35.6% CH₄ conversion) for 10 wt% MnTiO₃-NW/SG, and 21.5% (60.5% C₂₊ selectivity with 35.5% CH₄ conversion) for 20 wt% Mn-Ti-NW/SG. The activity of MnTiO₃-NW/CS gradually diminished as the MnTiO₃ loading exceeded 10 wt%, whereas the activities of MnTiO₃-NW/SG and Mn-Ti-NW/SG (both with the sol-gel SiO₂ support) hardly changed.

For the OCM reaction, designing a catalyst with high olefin selectivity is still challenging. Olefins, especially ethylene and propylene, have been important raw chemicals since the beginning of the chemical industry in the 1920s. Various downstream products of olefins, such as polyethylene, polypropylene, polyvinyl chloride, and ethanol, are utilized worldwide⁴⁴. In Table 1, the catalytic performance is presented in terms of olefins/paraffin selectivity and olefins/paraffin ratio. It is important to note that the number (5, 10, 15, and 20) preceding each catalyst name refers to the loading of MnTiO₃ or Mn-Ti, with “0wt%” omitted. The results indicated that NW/CS and NW/SG had relatively low olefins/paraffin ratios of 1.3 and 1.2, respectively. The 5MnTiO₃-NW/CS and 10MnTiO₃-NW/CS catalysts had relatively high olefins/paraffin ratios of 2.1, and 2.2, respectively, with the highest C₂₊ yield of 20.6%. When the MnTiO₃ amount increased over 10 wt%, the olefins/paraffin ratio slightly decreased, corresponding to a higher CO_x selectivity. For MnTiO₃-NW/SG and Mn-Ti-NW/SG, the olefins/paraffin ratios changed negligibly (2.2–2.3) as the amount of MnTiO₃ and Mn-Ti increased. The difference in the behaviors of olefins/paraffin ratio at high loadings could be related to the distribution of the active metals on each support. The active metals of the catalysts using SG could be more well-dispersed due to the high porosity of the SG (see more detail in the discussion of Scheme 1). Considering the performance between MnTiO₃-NW and Mn-Ti-NW on SG, at the same loading, the performance between these two had no significant difference, except at 5wt% loading 5MnTiO₃-NW/SG exhibited a slightly lower performance. The catalysts producing the maximum yield in each group (5MnTiO₃-NW/CS, 10MnTiO₃-NW/SG, and 20Mn-Ti-NW/SG) exhibited high levels of dehydrogenation resulting in olefins/paraffin ratios of 2.1–2.3. However, when considering the C₂₊ formation rate (r_{C₂₊})—total moles of C₂₊ per total moles of MnTiO₃ or (Mn + Ti) and Na₂WO₄ per h—of each catalyst (see Table 1), 5MnTiO₃-NW/CS, 5MnTiO₃-NW/SG, and 5Mn-Ti-NW/SG exhibited the highest r_{C₂₊} in each group. This suggests that the accessible active sites of the catalysts at high loadings (>5 wt%) are limited, possibly because of the low surface area and lack of pores of the catalysts. Nonetheless, this present work considers the catalyst performance in terms of C₂₊ yield per catalyst mass, and thus 5MnTiO₃-NW/CS, 10MnTiO₃-NW/SG, and 20Mn-Ti-NW/SG were chosen for further characterization.

Catalyst characterization. The most promising catalysts from Sect. “Activity of catalysts in the OCM reaction” were further analyzed to explain their performance via their properties. The selected catalysts included the basic catalysts (NW/CS and NW/SG), the catalysts producing the maximum yield in each group (5MnTiO₃-NW/CS, 10MnTiO₃-NW/SG, and 20Mn-Ti-NW/SG), and one other catalyst from each group (20MnTiO₃-NW/CS, 20MnTiO₃-NW/SG, and 5Mn-Ti-NW/SG).

The XRD patterns of these catalysts are collected in Supplementary Figure S2, with the assignment of XRD peaks to crystalline phases summarized in Supplementary Table S1. All catalysts exhibited XRD peaks



Scheme 1. Models for the stability of the catalysts using CS- and SG-supports.

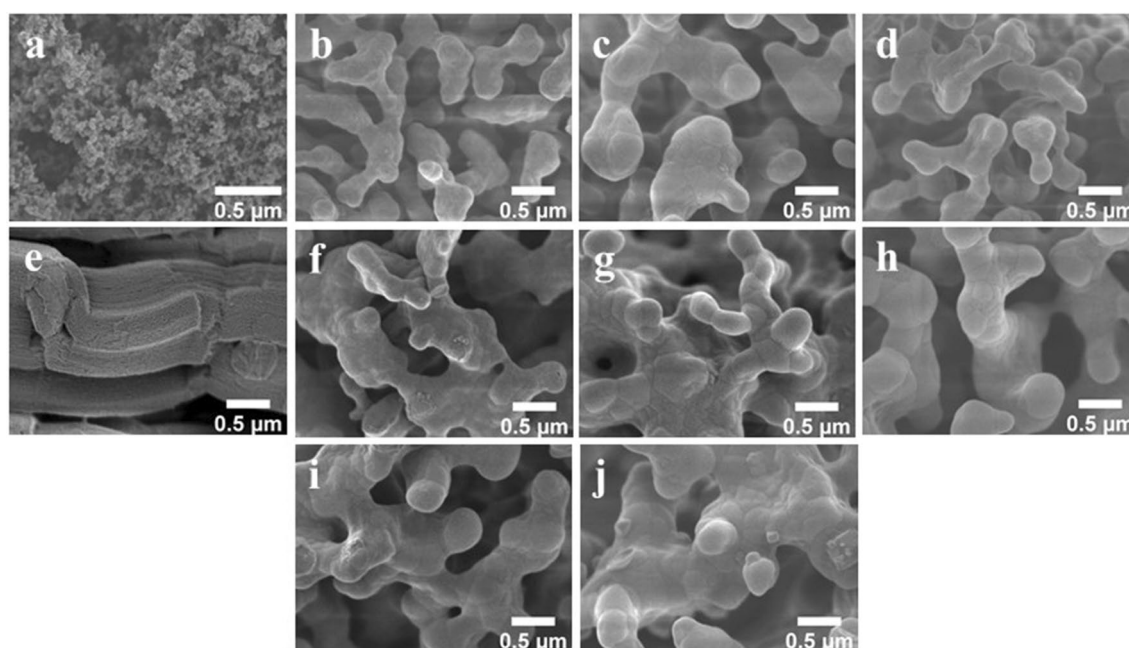


Figure 1. FE-SEM images of catalysts: (a) CS, (b) NW/CS, (c) 5MnTiO₃-NW/CS, (d) 20MnTiO₃-NW/CS, (e) SG, (f) NW/SG, (g) 10MnTiO₃-NW/SG, (h) 20MnTiO₃-NW/SG, (i) 5Mn-Ti-NW/SG, and (j) 20Mn-Ti-NW/SG.

characteristic of Na₂WO₄ and α -cristobalite. This confirmed the transformation of amorphous SiO₂ to α -cristobalite assisted by Na atoms, in line with the previous reports^{20,23,45}. Nevertheless, crystalline Mn₂O₃, Mn₃O₄, and TiO₂ were also detected, indicating that the MnTiO₃ particles partially decomposed into MnO_x and TiO₂ during catalyst preparation. The crystalline Mn₂O₃, Mn₃O₄, and TiO₂ phases were observed for the catalysts prepared with Mn and Ti. The MnTiO₃ phase was detected in all catalysts that were prepared with MnTiO₃. Weak signals of the α -tridymite phase in all catalysts and strong signals of quartz were perceived in 10wt% and 20wt%MnTiO₃-NW/SG. The catalytic tests (Table 1) indicate that the catalysts containing MnTiO₃, MnO_x, TiO₂, and α -cristobalite had high C₂₊ yields; thus, these crystalline phases seem essential in enhancing C₂₊ formation.

The morphology of the catalysts imaged by FE-SEM is presented in Fig. 1 and the average particle size of each catalyst determined using ImageJ software is presented in Supplementary Figure S3–S12 and Table S2–S11. The CS support appeared spherical with an average particle size of 34 nm (Fig. 1a), whereas SG contained multiple layers (average thickness of 0.4 μ m) with porosity (Fig. 1e). All prepared catalysts had similar coral-like particles. However, the average width of particles of catalysts prepared from CS (approximately 0.3–0.5 μ m) was somewhat smaller than those from SG (approximately 0.4–0.6 μ m). Upon the addition of different quantities of MnTiO₃ or Mn-Ti to the catalysts, the particle size and shape on the micrometer-scale changed negligibly. The elemental distribution and amount of Mn, Ti, Na, W, and Si in 10MnTiO₃-NW/SG (Fig. 2) and the other selected catalysts (Supplementary Table S12) were examined by FE-SEM with EDX. Each element was well-dispersed over the surface of the catalysts, which facilitated the activation of CH₄¹⁰.

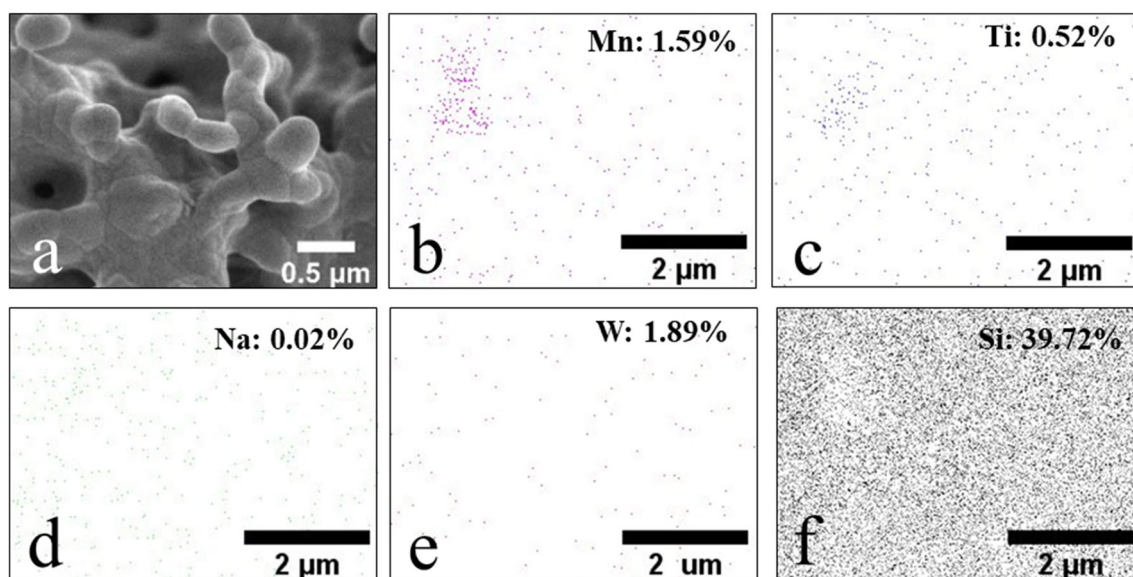


Figure 2. (a) FE-SEM and (b), (c), (d), (e), and (f) EDX images and weight percent each elemental of 10MnTiO₃-NW/SG.

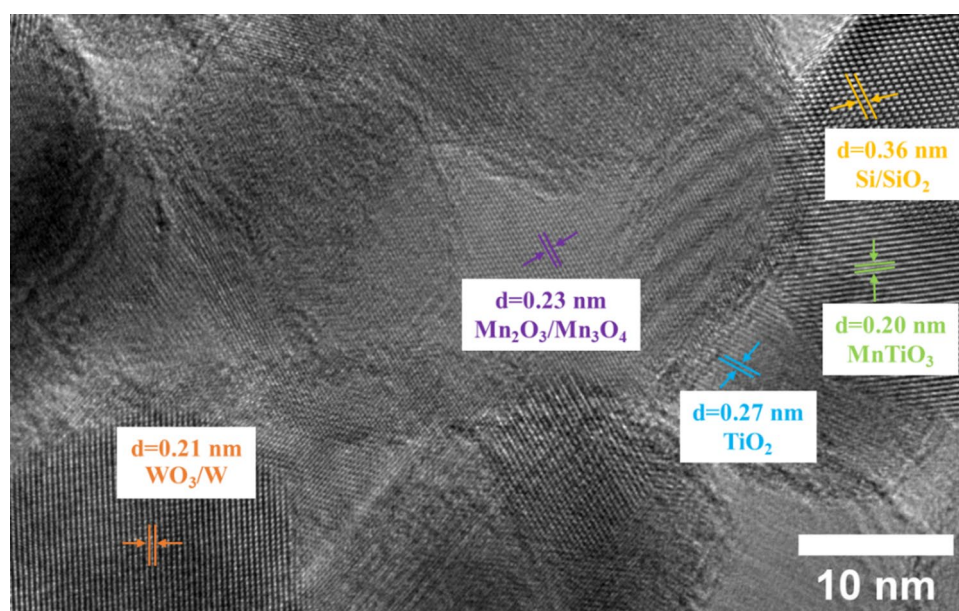


Figure 3. TEM image of 10MnTiO₃-Na₂WO₄/SG.

The structural morphologies of 10MnTiO₃-Na₂WO₄/SG were characterized using HR-TEM as shown in Fig. 3. As seen in Fig. 3, the active sites were distributed throughout the SG. The Si/SiO₂ had a lattice d-spacing of 0.36 nm, corresponding to the Si crystal lattice [1 1 0]⁴⁶. The lattice d-spacings of 0.20 and 0.27 nm corresponded to the crystal plane of MnTiO₃ [1 1 0]⁴⁷ and TiO₂ [1 0 1]⁴⁷, respectively. The WO₃/W had a lattice d-spacing of 0.21 nm, relating to the lattice plane of WO₃/W [2 0 1]⁴⁸. The Mn₂O₃ and Mn₃O₄ had a lattice d-spacing of 0.23 nm, corresponding to the crystal plane of Mn₂O₃ [1 1 1]⁴⁹ and Mn₃O₄ [0 1 0]⁵⁰. The HR-TEM results confirm that the active phases distributed throughout the SG support and 10MnTiO₃-Na₂WO₄/SG are nanocomposite due to the nano-scale structures⁵¹.

The BET surface area, pore-volume, and pore size of all catalysts determined by N₂-physisorption are presented in Table 2 (isotherms are shown in Supplementary Figure S13). SG had the highest BET surface area (409.2 m² g⁻¹), followed by CS (89.6 m² g⁻¹). After using the supports for catalyst preparation, the BET surface areas were largely reduced (0.7–5.7 m² g⁻¹). The surface area of similar catalysts was also reduced after calcination (2.9–8.6 m² g⁻¹; amorphous SiO₂ support 89.6 m² g⁻¹)^{10,38}. The tremendous reduction of the surface area of the supports (i.e., SG and CS) generally occurs when preparing a catalyst containing Na₂WO₄/SiO₂. This is because the structure of the support (e.g., porous material and/or nanoparticle) has completely changed from

Catalyst	BET surface area ($\text{m}^2 \text{g}^{-1}$)	Pore volume ($\text{cm}^3 \text{g}^{-1}$)	Pore size (nm)
CS	89.6	-	-
NW/CS	5.7	-	-
5MnTiO ₃ -NW/CS	3.2	-	-
20MnTiO ₃ -NW/CS	0.7	-	-
SG	409.2	0.545	5–10
NW/SG	3.8	-	-
10MnTiO ₃ -NW/SG	1.7	-	-
20MnTiO ₃ -NW/SG	1.8	-	-
5Mn-Ti-NW/SG	3.2	-	-
20Mn-Ti-NW/SG	3.4	-	-

Table 2. BET surface area, pore volume, and pore size of catalysts.

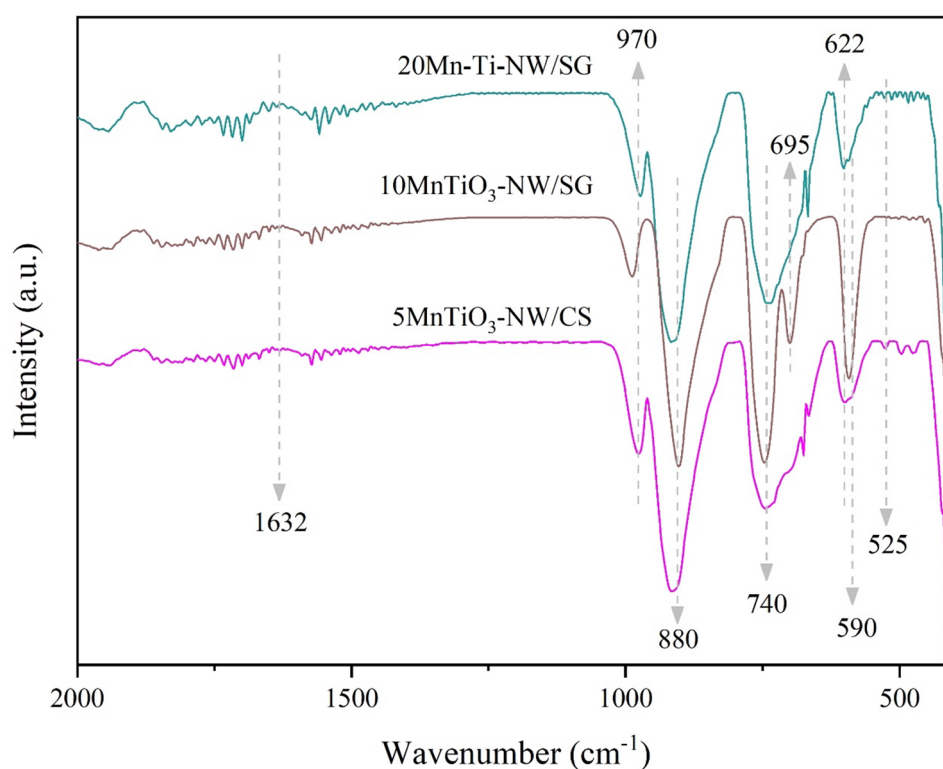


Figure 4. FTIR spectra of selected catalysts.

nanoparticles (30–50 nm) to large grain sizes (approximately 0.2–1.0 μm) as indicated by the SEM images in Fig. 1 of an α -cristobalite-containing catalyst without internal pores (i.e., non-porous material)^{27,52}. Thus, a very small surface area (e.g., $< 6 \text{ m}^2/\text{g}$) is obtained. The catalysts containing MnTiO₃ exhibited smaller surface areas, pore-volumes, and pore sizes than those without MnTiO₃. Similarly, the addition of Mn + Ti produced catalysts with a small surface area (3.2–3.4 $\text{m}^2 \text{g}^{-1}$), but still larger than those containing MnTiO₃. Nevertheless, there was a negligible difference between the pore volumes and pore sizes of catalysts with and without Mn + Ti. Moreover, the increased loading of MnTiO₃ from 10 to 20 wt% on NW/SG or Mn + Ti from 5 to 20 wt% on NW/SG did not significantly change the surface area. Based on the N₂-physisorption isotherm analysis in Supplementary Figure S13, and according to the IUPAC classification, the SG support is specified as type IV (mesoporous material, containing pore size of 5–10 nm) with H1 hysteresis, while the CS support and all the prepared catalysts showed an indistinct hysteresis loop. However, after careful analysis of the plots shown as inserts of Supplementary Figure S13 and the SEM images (Fig. 1), the CS support and the catalysts appeared to be non-porous with rough surfaces, which would be classified as type II (nonporous material).

The FTIR patterns of selected catalysts producing the maximum yield in each group (5MnTiO₃-NW/CS, 10MnTiO₃-NW/SG, and 20Mn-Ti-NW/SG) are displayed in Fig. 4. The FTIR peaks at 970, 880, and 740 cm^{-1} correspond to Si–O–(H–H₂O)²⁸, Si–OH⁵³, and Si–O–C^{54,55} bonds, respectively. The FTIR peak at 622 cm^{-1} for all

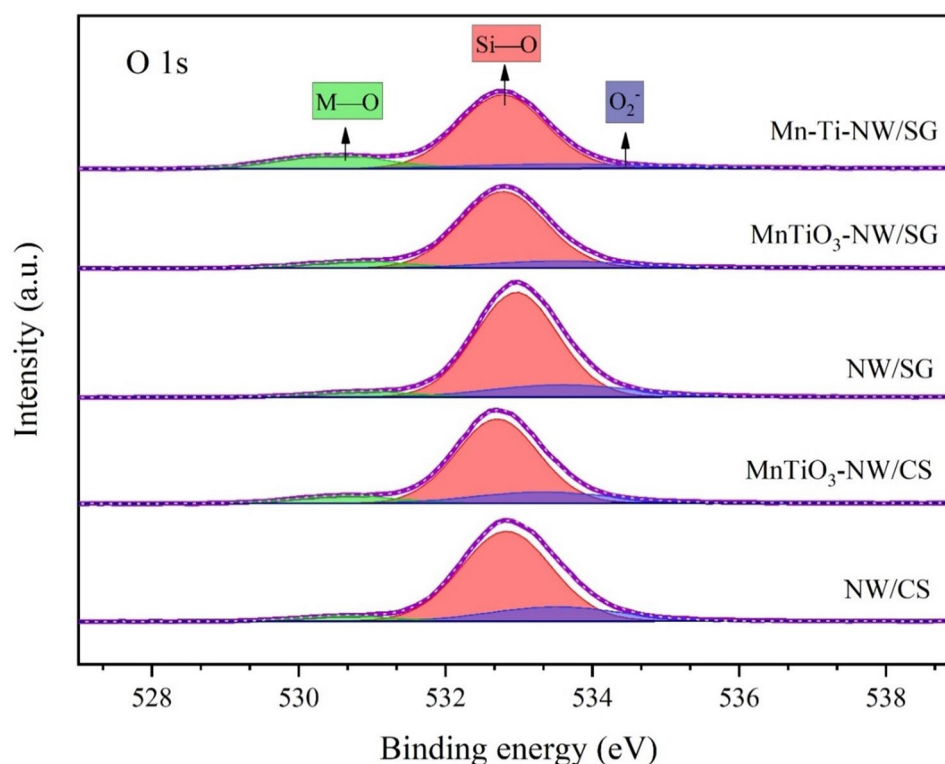


Figure 5. XPS spectra in the O 1s region for different catalysts.

Catalyst	Binding energy (eV)		
	O1s, (FWHM), and relative amount (%)		
	^a M–O	Si–O	O ₂ ^{•−}
NW/CS	530.6 (1.5) 4.9	532.8 (1.4) 77.4	533.5 (2.1) 17.6
MnTiO ₃ -NW/CS	530.6 (1.6) 8.7	532.7 (1.3) 74.9	533.3 (2.1) 16.4
NW/SG	530.9 (1.5) 5.1	532.9 (1.3) 79.3	533.6 (2.3) 15.7
MnTiO ₃ -NW/SG	530.8 (1.7) 8.8	532.8 (1.4) 79.1	533.5 (2.3) 12.0
Mn-Ti-NW/SG	530.5 (1.8) 17.4	532.8 (1.4) 72.7	533.6 (3.1) 9.9

Table 3. Curve-fitted and quantified O 1s XPS results of catalysts. ^a M–O (M = Na, W, Mn, or Ti): FWHM = Full width at half maximum.

catalysts characterizes α -cristobalite SiO₂^{45,56}. Previous studies suggested that the amorphous SiO₂ can transform to the α -cristobalite SiO₂ at 800 °C if Na is present during the calcination^{20,21}. To confirm that, CS, Na/CS, and NW/CS were prepared using the same procedure as 5MnTiO₃-NW/CS and analyzed using FTIR as shown in Supplementary Figure S14. The peak at 622 cm^{−1} that specifies the α -cristobalite SiO₂ phase was also observed when Na was present (i.e., Na/CS and NW/CS). This is in good agreement with the reports²¹. An FTIR peak at 695 cm^{−1} was only observed for 10MnTiO₃-NW/SG, indicating the presence of quartz (SiO₂)⁵⁶. The FTIR peak at 525 cm^{−1} is associated with the bending vibration mode of O–Mn–O⁵⁷, indicating the presence of MnO₂. The intense peak at 590 cm^{−1} originates from the vibration of the O–Ti–O bond⁵⁸, which was detected in the TiO₂-containing catalyst. The peak at 1632 cm^{−1} was assigned to the O–H bending mode, due to moisture⁵⁹.

The surface composition of the catalysts was analyzed by XPS (Supplementary Table S13 and Supplementary Figure S15–S19). The curve-fitted and quantified XPS peaks of Na 1s, W 4f, Si 2p, Ti 2p, and Mn 2p are presented in Supplementary Table S13. The XPS peaks were considered as a mixture of Gaussian and Lorentzian functions (80:20 ratio)⁶⁰. Na is a component of Na₂WO₄ (Supplementary Figure S15). The binding energies of W 4f_{7/2} and W 4f_{5/2} (Supplementary Figure S16) in every catalyst indicated the presence of WO₄^{2,23}. The peaks of Si 2p (Supplementary Figure S17) correspond to SiO₂. The binding energies of Mn 2p (Supplementary Figure S18) and Ti 2p (Supplementary Figure S19) for nanocomposite MnTiO₃-NW/CS and MnTiO₃-NW/SG were different from those of nanocomposite Mn-Ti-NW/SG.

In the OCM mechanism, the oxygen species are crucial for CH₄ activation. The XPS spectra and the O 1s binding energies of the different catalysts are presented in Fig. 5 and Table 3, respectively. Overall, three types

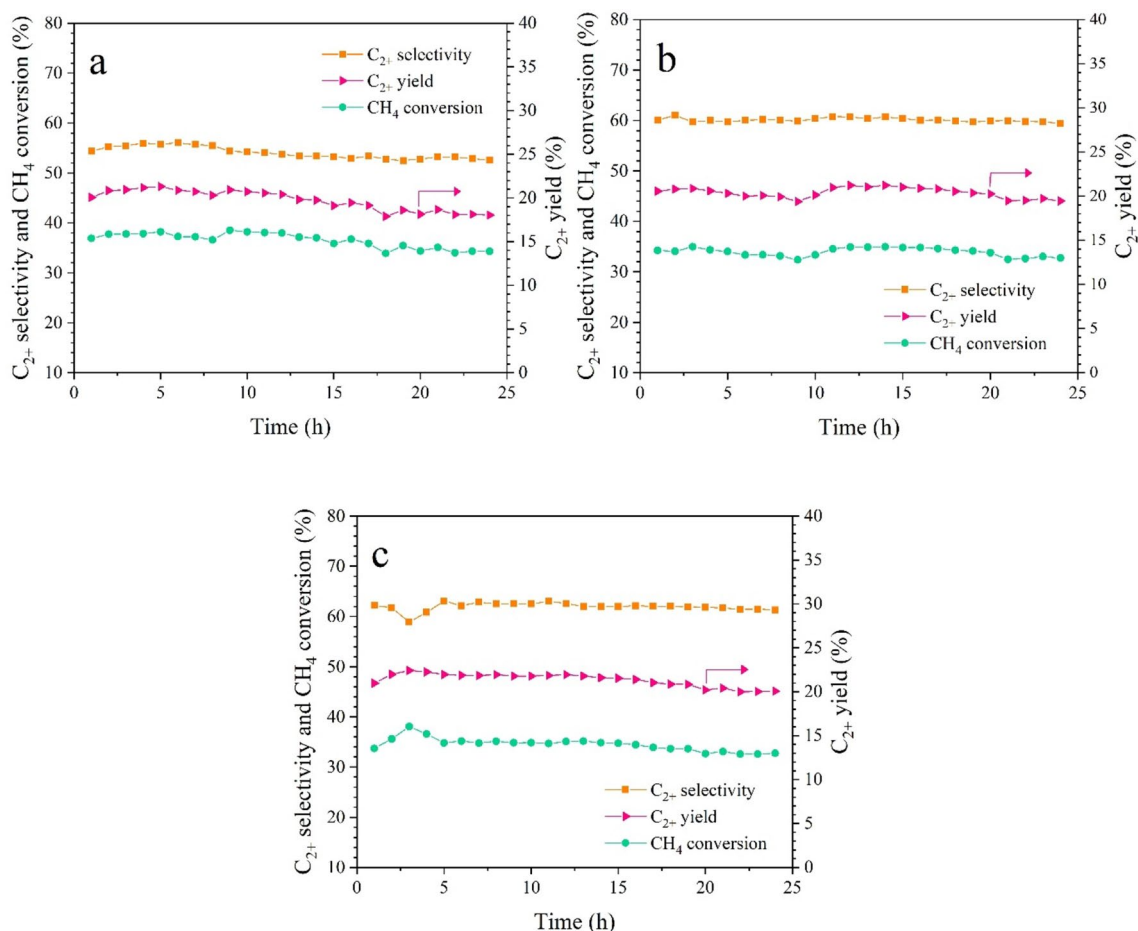


Figure 6. Catalytic performance in OCM reaction: (a) MnTiO₃-NW/CS, (b) MnTiO₃-NW/SG, and (c) Mn-Ti-NW/SG catalysts over 24 h. Conditions: 50 mg catalyst, gas feed of CH₄:O₂:N₂ = 3:1:4, reactor temperature = 700 °C, atmospheric pressure, total feed gas flow rate = 50 mL min⁻¹ (GHSV = 30,588 h⁻¹).

of oxygen species were identified: oxygen of M–O species at 530.5–530.9 eV, oxygen of Si–O at 532.7–532.9^{61,62}, and O₂⁻ at 533.3–533.6 eV⁶³. M–O represents the oxygen species of Na–O at 530.8 eV⁶⁴, W–O at 530.6 eV⁶⁴, and Mn–O at 530.3 eV⁶⁵, and Ti–O showing two peaks at 530.0 and 531.8 eV⁶⁴. The peaks around 530.5–530.9 eV for M–O in NW/CS and NW/SG were relatively small (as NW/CS and NW/SG had no components of Mn–O and Ti–O), while relatively large peaks were observed for MnTiO₃-NW/CS, MnTiO₃-NW/SG, and Mn-Ti-NW/SG. The O⁻, and O₂⁻ lattice species are essential for CH₄ activation^{66,67}, whereas the O²⁻ lattice species leads to complete oxidation of hydrocarbon products to CO_x⁶⁰. Based on the activity results in Fig. 5, catalysts containing M–O (i.e., XPS peak around 530.5–530.9 eV) exhibited high CH₄ conversion. This implied that a catalyst with this specific oxygen species promotes CH₄ activation as the lattice oxygen of the catalyst surface is easily reacted and re-populated (high oxygen mobility).

Stability of catalysts in the OCM reaction. The stability of 10MnTiO₃-NW/CS, 5MnTiO₃-NW/SG, and 20Mn-Ti-NW/SG, catalysts that had produced the highest C₂₊ yields, was further tested for over 24 h (Fig. 6). The three catalysts had similar performance with the maximum C₂₊ yield (~21–23%) obtained within 3–4 h. After that, performance slightly diminished, especially for CH₄ conversion and C₂₊ yield. The reduction levels in terms of C₂₊ yield for MnTiO₃-NW/CS (Fig. 6a), MnTiO₃-NW/SG (Fig. 6b), and Mn-Ti-NW/SG (Fig. 6c) were 15.3%, 8.4%, and 10.5%, respectively. Moreover, 20wt% Mn-Ti-NW on CS (20Mn-Ti-NW/CS) was prepared and tested for reaction to compare its performance with that of 20Mn-Ti-NW/SG (see Supplementary Figure S20). As observed, the activity of Mn-Ti-NW/CS decreased faster than the other catalysts, similar to the previous reports^{27,37–39}. This confirms that the MnTiO₃-NW/SG catalyst was the most active and durable catalyst among all prepared.

The XRD patterns of fresh and used catalysts are presented in Fig. 7 (for peaks assignments see Supplementary Table S1). Some XRD peaks indicated changes. First, the Na₂WO₄ peaks in used MnTiO₃-NW/CS and Mn-Ti-NW/SG catalysts had disappeared, which could be a result of the destruction of crystalline Na₂WO₄^{11,68,69}. This may be related to the reduction in catalytic activity. Second, the quartz phase was found in the used MnTiO₃-NW/CS catalyst and the presence of α-tridymite became more pronounced in the used Mn-Ti-NW/SG. Thus, the activity of the catalysts was reduced, because these two phases do not promote methane activation. For the

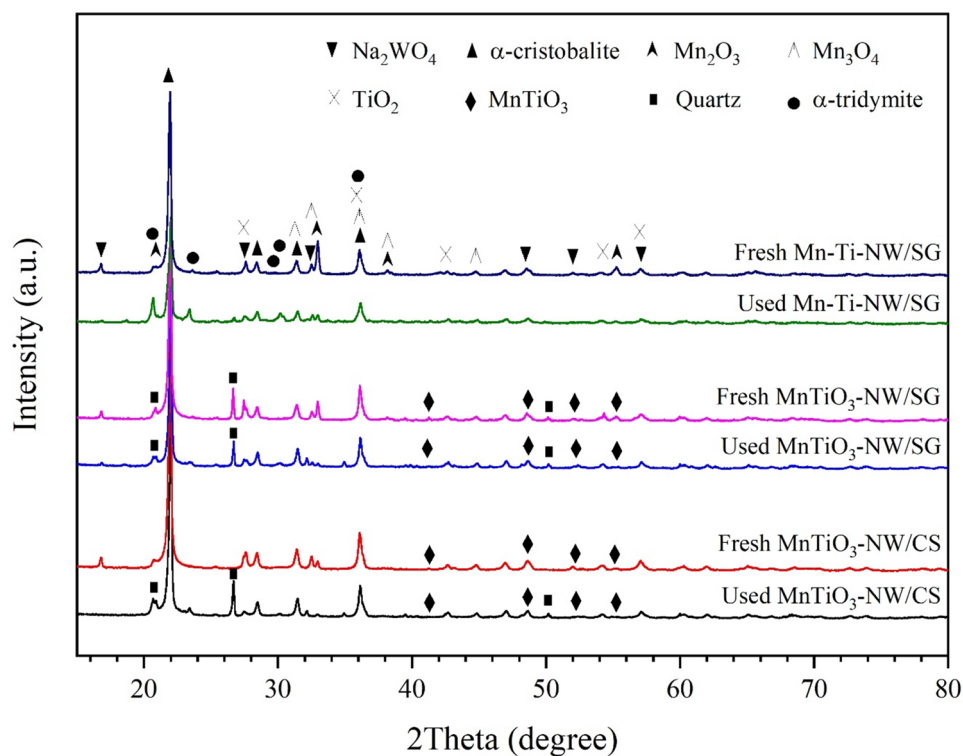


Figure 7. XRD patterns of fresh and used (24 h) catalysts.

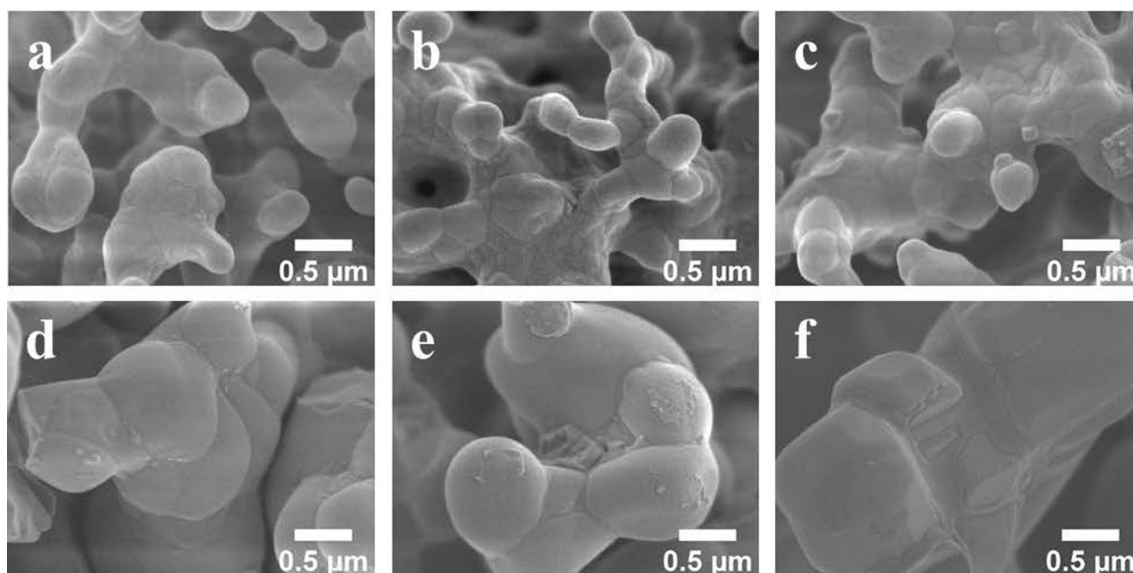


Figure 8. FE-SEM images of fresh and used catalysts: (a) Fresh MnTiO₃-NW/CS, (b) Fresh MnTiO₃-NW/SG, (c) Fresh Mn-Ti-NW/SG, (d) Used MnTiO₃-NW/CS, (e) Used MnTiO₃-NW/SG, and (f) Used Mn-Ti-NW/SG.

MnTiO₃-NW/SG catalyst, the XRD peaks after reaction remained practically unaffected, confirming the excellent catalytic stability of MnTiO₃-NW/SG with no activity loss as changes in crystalline phases were absent.

The morphologies of fresh and used catalysts were analyzed by FE-SEM (Fig. 8) and the average particle size of used catalysts were determined using ImageJ software and is presented in Supplementary Figure S21–S23 and Table S14–S16. The metal distribution of each catalyst was also characterized by FE-SEM with EDX (Supplementary Table S12). When the FE-SEM images of fresh and used (24 h) catalysts were compared, the particle shapes appeared very similar. Nevertheless, the particle size of each used catalyst (approximately 1.2–1.6 μm) was more than double of each fresh catalyst (approximately 0.3–0.6 μm). This is paralleled by a reduction in

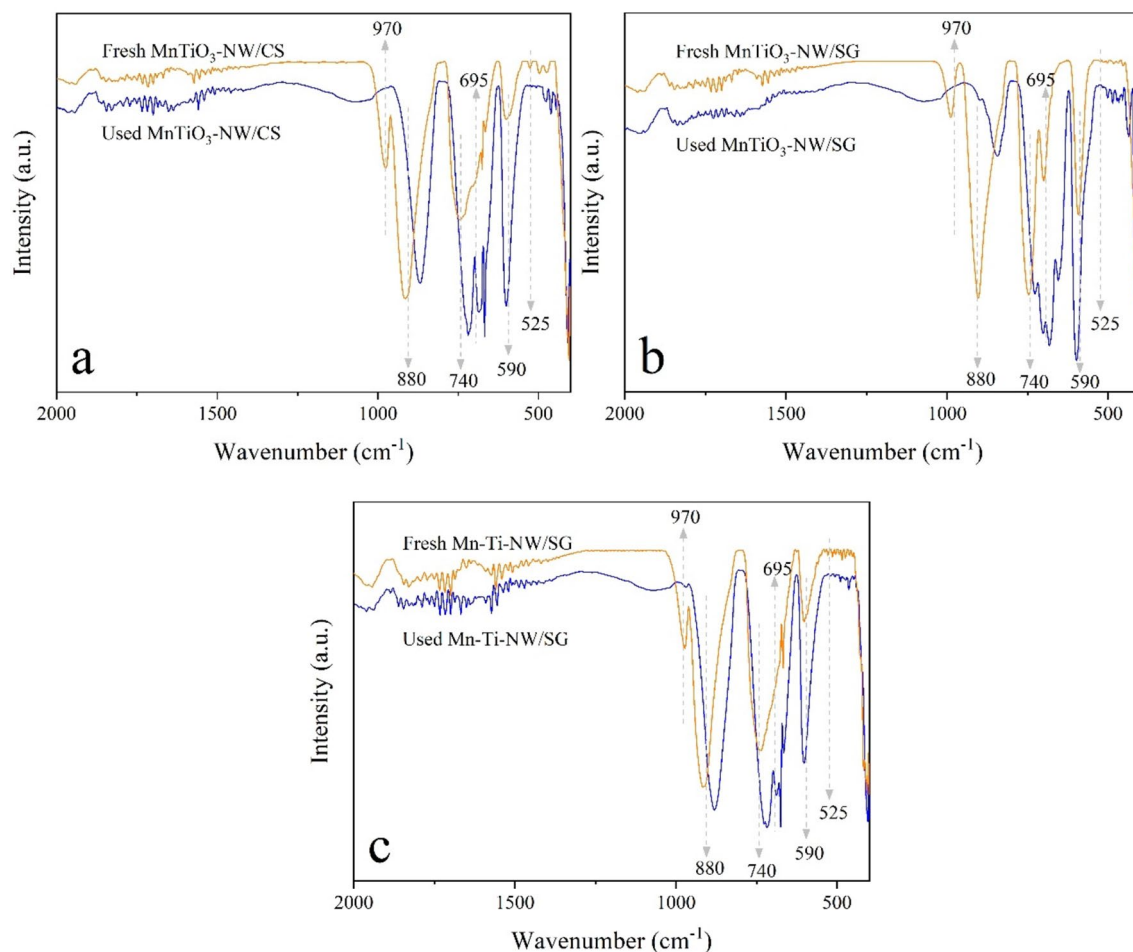


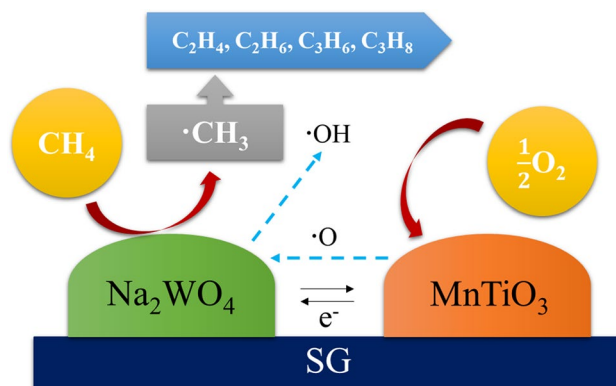
Figure 9. FTIR spectra of fresh and used catalysts: (a) 5MnTiO₃-NW/CS, (b) 10MnTiO₃-NW/SG, and (c) 20Mn-Ti-NW/SG.

surface area, so that performance in OCM decreased after testing for several hours. Moreover, the increase in particle size may also result in a partial loss of the catalytic interface between the active components for activating methane (i.e., Na₂WO₄ and Mn₂O₃)^{68,69}, thereby causing decreased catalytic activity. The EDX images of the used catalysts (Supplementary Table S12) indicated the presence of Mn, Ti, Na, and W elements on the catalyst surface. The distribution and concentration of the active elements did not significantly change, in good accordance with the stability tests.

Another reason why the catalysts prepared using SG were more stable than those using CS is presented in Scheme 1. According to the textural properties in Table 2, SG has a larger surface area with high porosity, while CS has no internal pores. Thus, during impregnation, the active components were impregnated inside the pores of SG before the transformation of amorphous SiO₂ to α -cristobalite, so that the active components were widely dispersed inside the catalyst's pores. In contrast, the active components impregnated on CS were dispersed only over the surface of CS (like a thin film coating⁶⁹), since it is non-porous (see CS in Scheme 1). According to some reports, the crystalline phase of Na₂WO₄ disappeared due to slow evaporation within several hours of the stability test^{11,68,69} and/or it transforms to another phase (MnWO₄)⁶⁸. Notably, the melting temperature of Na₂WO₄ is 698 °C, while the reaction temperature for OCM is over 700 °C due to exothermicity¹¹. Therefore, it seems easier to lose Na₂WO₄ from the CS-supported than from the SG-supported catalyst.

The FTIR spectra of fresh and used catalysts are shown in Fig. 9. After the catalysts had been used, the FTIR peak of Si–O–(H–H₂O) disappeared, suggesting that the H₂O attached to Si–O–H was removed. Additionally, there was an FTIR peak appearing at 695 cm⁻¹, indicating the presence of quartz (SiO₂)⁵⁶. The quartz phase was detected in the fresh MnTiO₃-NW/SG and was clearly visible in all used catalysts, which is in good agreement with the XRD results in Fig. 7. This suggested that the α -cristobalite phase slowly transformed into the quartz phase. The FTIR peak at 524 cm⁻¹ was assigned to the bending vibration of O–Mn–O⁵⁷ and it was detected in each catalyst. The intense peak at 590 cm⁻¹ was the vibration of the O–Ti–O bond⁵⁸, which was also perceived in each catalyst.

The plausible mechanism of this reaction over MnTiO₃-NW/SG is illustrated in Scheme 2. The most possible active site for the CH₄ activation is the lattice oxygens of WO₄^{2,30}. During the CH₄ activation to CH₃ radical by the lattice oxygens, W⁶⁺ is reduced to W⁵⁺³⁰. The CH₃ radical is then coupled with another CH₃ radical to yield C₂H₆ in the gas phase, which can further generate C₂H₄ and other hydrocarbons via the C–H activation and dehydrogenation over the catalyst surface. However, the oxidation of CH₄ can occur at the same temperature



Scheme 2. Mechanism of OCM over MnTiO₃-NW/SG.

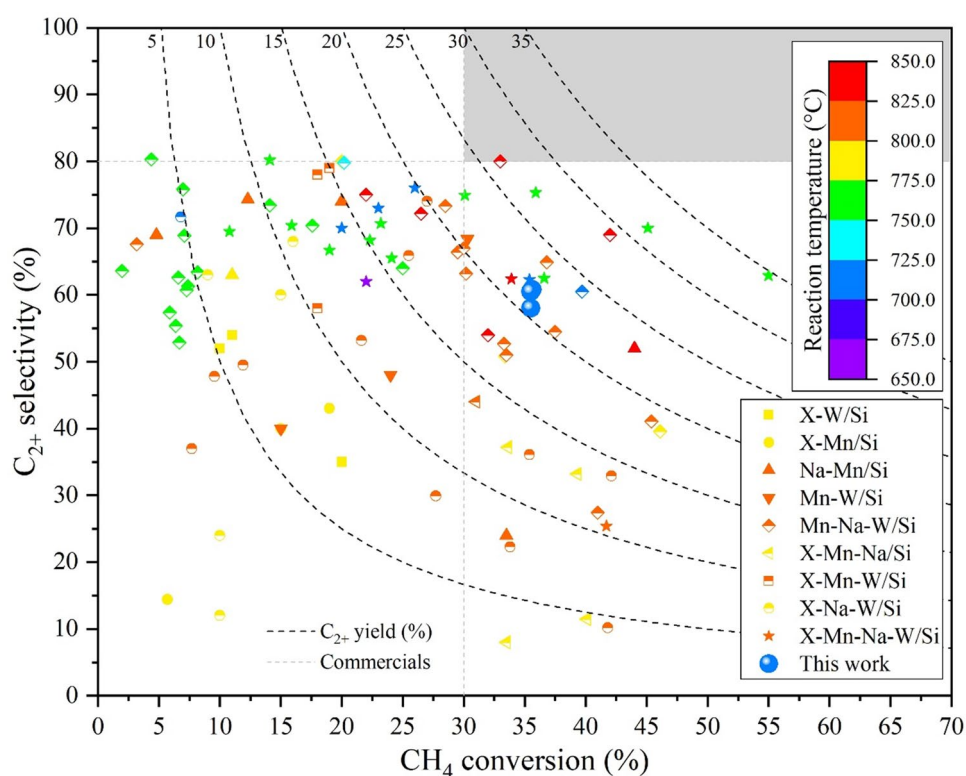


Figure 10. Survey of various catalysts reported in the literature, including the current ones. The gray area in the top right-hand corner indicates the target zone for commercially viable catalyst performance.

(600–1,000 °C) to produce CO and CO₂. A sketch of the mechanisms and series of OCM reaction, CH₄ oxidation, and dehydrogenation are presented in Supplementary Information equations (S1)–(S14)¹⁹. At the same time, due to the facile mobility of the lattice oxygen of Mn–O species²⁷, the lattice oxygen from MnTiO₃ is transferred to the WO₄²⁻ species. As a result, Mn²⁺ is oxidized to Mn³⁺. After that, the O₂ molecule from the gas phase is adsorbed onto the surface of MnTiO₃ and the OH radical is released from the WO₄²⁻ surface. An electron exchange from W⁵⁺ to Mn³⁺ simultaneously occurs, which regenerates W⁶⁺ and Mn²⁺, and is ready for the new cycle of the reaction.

A survey of various catalysts reported in the literature for the OCM reaction is presented in Fig. 10, with the details of each catalyst described in Supplementary Table S17. The activity of OCM catalysts should be over 30% CH₄ conversion and 80% C₂₊ selectivity⁷ to have the potential for commercial exploitation (indicated by the gray area in Fig. 10). The catalysts studied herein are outside the required area; specifically, as their C₂₊ selectivity is below 80%. Several reported catalysts also had a CH₄ conversion above 30% with a C₂₊ selectivity below 80%, however, all of them were used at a temperature above 750 °C. Thus, in light of the lower temperature (700 °C), our present catalysts exhibited good performance. Nevertheless, further improvement is necessary, especially

increasing C_{2+} selectivity above 80% while maintaining the CH_4 conversion. Some Mn-Na-W/Si and X-Na-W/Si catalysts have a C_{2+} selectivity of around 80% at a reaction temperature of 725–775 °C, but they have low CH_4 conversions (4.4–20.2%)^{15–17,31}. No catalyst based on Na, W, and/or Mn can provide a C_{2+} selectivity above 81%, implying that improving the C_{2+} selectivity while maintaining the CH_4 conversion above 30% is very challenging. Remarkably, one report in 1998 showed that an Mn-Na-W/Si catalyst performed well in the OCM reaction, producing C_{2+} selectivity of 80% and CH_4 conversion of 33% (for a yield of 26.4%) at a reaction temperature of 850 °C²⁰. Nevertheless, thereafter such high performance of the same catalyst was not reported. The addition of additives to Mn-Na-W/Si (as X-Mn-Na-W/Si) can improve the C_{2+} selectivity to about 62–75% with a CH_4 conversion above 30%. When X = NaCl, the highest C_{2+} yield reported was 34.6% (62.9% C_{2+} selectivity and 55% CH_4 conversion)¹⁷, but the catalysts were not stable for long periods due to a loss of chloride. The performance of our catalysts containing Mn, Na, and W components upon using SiO_2 as catalyst support has been improved, identifying several key factors, but a viable catalyst for industrial use is still at large.

Conclusion

Different loadings of nanocomposite $MnTiO_3$ -NW or MnO_x - TiO_2 -NW supported on silica (CS and SG) were successfully prepared and tested in the OCM reaction. The highest C_{2+} yields were obtained for 10MnTiO₃-NW/SG (21.6%), followed by 20Mn-Ti-NW/SG (21.5%), and 5MnTiO₃-NW/CS (20.6%). These catalysts produced high levels of dehydrogenation, generating olefins/paraffin ratios of 2.1–2.3. Catalysts characterization by XRD detected $MnTiO_3$, MnO_x , TiO_2 , and α -cristobalite phases, while using XPS identified oxygen species of M–O (M = Na, W, Mn, and Ti) that were strongly related to high CH_4 conversion and high C_{2+} yield. Considering the catalytic activity between $MnTiO_3$ -NW and Mn-Ti-NW on the same support (i.e., SG), a small activity difference was observed between these two when the metal loading at 5wt%, in which the activity of 5MnTiO₃-NW/SG was lower than that of 5Mn-Ti-NW/SG, while they perceived no substantial difference in the activity at the higher loadings. Comparing the type SiO_2 support, the activity results presented that the catalysts with porous SG support were more stable than those with non-porous CS as support. The gradual catalyst deactivation observed during the stability test, especially for the catalyst with CS, was mainly due to the destruction of crystalline Na_2WO_4 . Therefore, further improvement of catalytic performance seems to require an alternative active component that is retained under harsh operating conditions.

Methods

Catalysts preparation. *Preparation of $MnTiO_3$ nanocatalysts.* The $MnTiO_3$ catalyst was prepared using the stearic acid gel method⁷⁰. In the first step, stearic acid (0.4 mol, $C_{18}H_{36}O_2$, 98%, PanReac AppliChem) was heated in a beaker at 90 °C until it melted. After that, manganese acetate (0.1 mol, $Mn(OOCCH_3)_2 \cdot 4H_2O$, Mn 22%, Alfa Aesar) was added dropwise. The mixture was continuously stirred for 8 h to form a dark brown solution. Then, tetra butyl titanate (0.1 mol, $Ti[O(CH_2)_3CH_3]_4$, $\geq 97.0\%$, Sigma-Aldrich) was added dropwise to the mixture upon continuous stirring for 1 h to form a homogeneous brown liquid. Next, the mixture was dried in an oven at 100 °C for 12 h. Finally, the dried gel was calcined in four stages in the air (KJ-M1200-27L, Kejia furnace). In the first stage, the dried gel was heated to 400 °C with a heating rate of 1 °C min^{-1} . Second, the temperature was held at 400 °C for 40 min. Third, the temperature was ramped up to 800 °C with a heating rate of 3 °C min^{-1} . Finally, the temperature was held at 800 °C for 2 h and then slowly cooled down to room temperature⁷⁰. The crystalline $MnTiO_3$ sample was ground to obtain a fine powder.

Preparation of the sol-gel SiO_2 support. Pluronic P123 (0.0005 mol, with an average molecular weight of ~ 5800, Aldrich) was dissolved in DI water (101 mL) with concentrated HCl (6.72 mL, 37%, Rankem). The mixture was continuously stirred at 40 °C until a clear solution was obtained. Then, tetraethyl orthosilicate (TEOS; 0.03 mol, $(C_2H_5O)_4Si$, $\geq 99.0\%$, Aldrich) was added to the mixture followed by continuous stirring for 4 h at 40 °C. After that, the mixture was dried overnight in a hot-air oven at 100 °C. Next, the dried sample was washed with DI water (150 mL) and dried again in a hot-air oven at 100 °C for 12 h. Finally, the dried sample was calcined in air at 550 °C for 3 h with a heating rate of 3 °C min^{-1} . The calcined sample was used as the sol-gel SiO_2 support.

Preparation of $MnTiO_3$ - Na_2WO_4 nanocomposites on silica. The silica-supported $MnTiO_3$ - Na_2WO_4 catalyst was prepared using the impregnation method. The synthesized sol-gel SiO_2 support and a commercial fumed SiO_2 (c- SiO_2 , amorphous fumed, a specific surface area of 85–115 $m^2 g^{-1}$, Alfa Aesar) were used. Initially, sodium tungsten hydrate ($Na_2WO_4 \cdot 2H_2O$, 98.0–101.0%, Daejung) was dissolved in DI water to have a concentration of 0.05 M. The prepared catalysts had loadings of 5.0 wt% of Na_2WO_4 and 0.0–20.0 wt% $MnTiO_3$ for each support. Accordingly, different amounts of $Na_2WO_4 \cdot H_2O$ solution and fine $MnTiO_3$ powder were loaded on each support. After mixing, the solution was continuously stirred at room temperature for 1 h. Then, the mixture was dried in hot-air at 100 °C for 1 h. The dried mixture was finally calcined in the air furnace at 800 °C for 4 h with a heating rate of 2 °C min^{-1} . The obtained catalysts were $MnTiO_3$ - Na_2WO_4 /c- SiO_2 (denoted as $MnTiO_3$ -NW/CS) and $MnTiO_3$ - Na_2WO_4 /sol-gel SiO_2 (denoted as $MnTiO_3$ -NW/SG). A commercial fumed silica with a surface area of 350–420 m^2/g was purchased and used to prepare a parallel catalyst with 5MnTiO₃- Na_2WO_4 /CS to check if another amorphous fumed silica having a specific surface area greater than 85–115 $m^2 g^{-1}$ gives different performance. The performance test results of two catalysts having the same active components and loading but the difference in specific surface areas (see Supplementary Table S18) showed no significant difference in the OCM performance.

Preparation of MnO_x - TiO_2 - Na_2WO_4 nanocomposites on sol-gel SiO_2 . The MnO_x - TiO_2 - Na_2WO_4 nanocomposite supported on the synthesized sol-gel SiO_2 was also prepared using the impregnation method. The sodium

tungsten dehydrate and manganese (II) nitrate tetrahydrate ($\text{Mn}(\text{NO}_3)_2 \cdot 4\text{H}_2\text{O}$, 97%, Chem-Supply) precursors were dissolved in DI water at concentrations of 0.05 M and 0.16 M, respectively, and the titanium (IV) isopropoxide ($\text{Ti}[\text{OCH}(\text{CH}_3)_2]_4$, $\geq 97.0\%$, Alfa Aesar) precursor was dissolved in ethanol ($\text{C}_2\text{H}_6\text{O}$, 99.9%, QREC) at a concentration of 0.07 M. Again, the concentration of Na_2WO_4 was fixed at 5 wt% and the amounts of Mn and Ti were adjusted to yield the same concentrations of MnTiO_3 (in molar ratio) as the catalysts in Sect. 4.1.3. This approach allowed for a meaningful comparison of catalytic activity among the prepared catalysts. After all the precursor solutions were added to the synthesized sol-gel SiO_2 support, the mixture was continuously stirred at room temperature for 1 h. The mixed solution was then dried in hot-air at 100 °C for 1 h and finally calcined in the air at 800 °C for 4 h with a heating rate of 2 °C min^{-1} . The so-obtained catalyst was a nanocomposite of MnO_x - TiO_2 - Na_2WO_4 /sol-gel SiO_2 (denoted as Mn-Ti-NW/SG).

Catalyst activity testing. The catalytic activity of each prepared catalyst in the OCM reaction was evaluated in a plug flow reactor. A catalyst (50 mg) was packed in a borosilicate glass tube with an inner diameter of 5 mm and sandwiched between layers of quartz wool. The feed gases were methane (CH_4 , 99.999% HP, Labgaz), oxygen (O_2 , 99.999% HP, Linde), and nitrogen (N_2 , 99.999% UHP, Labgaz). The feed gas ratio of CH_4 : O_2 : N_2 was 3:1:4 at a total feed flow rate of 50 mL min^{-1} (GHSV = 30,558 h^{-1}), which was fed into the plug flow reactor (Kejia furnace KJ-TI200). All flow rates were controlled using mass flow controllers (Aalborg GFC17) and double-checked using a bubble flow meter. The operating conditions were atmospheric pressure and a reactor temperature of 700 °C. The catalyst activity was evaluated 1 h after the system had reached the established conditions. The quantification of the gas products was carried out by gas chromatography (SHIMADZU, GC-14A) using Unibead C column connected with a thermal conductivity detector (TCD) for determining CO , CO_2 , and CH_4 and Porapak Q column connected with a flame ionization detector (FID) for determining C_2H_4 , C_2H_6 , C_3H_6 , C_3H_8 , C_4H_8 , and C_4H_{10} . A standard calibration curve for each product was established using five calibration points with a coefficient of determination (R^2) > 0.995. The activity of each catalyst is presented in terms of % CH_4 conversion, % C_{2+} selectivity, % CO_x selectivity, % C_{2+} yield, olefins/paraffin ratio (mol/mol), and C_{2+} formation rate ($r_{\text{C}_{2+}}$), which were calculated using Eqs. (1)–(6), respectively.

$$\% \text{CH}_4 \text{ conversion} = \frac{2(n_{\text{C}_2\text{H}_4} + n_{\text{C}_2\text{H}_6}) + 3(n_{\text{C}_3\text{H}_6} + n_{\text{C}_3\text{H}_8}) + 4(n_{\text{C}_4\text{H}_{10}}) + n_{\text{CO}} + n_{\text{CO}_2}}{2(n_{\text{C}_2\text{H}_4} + n_{\text{C}_2\text{H}_6}) + 3(n_{\text{C}_3\text{H}_6} + n_{\text{C}_3\text{H}_8}) + 4(n_{\text{C}_4\text{H}_{10}}) + n_{\text{CO}} + n_{\text{CO}_2} + n_{\text{CH}_{4,\text{out}}}} \times 100 \quad (1)$$

$$\% \text{C}_{2+} \text{ selectivity} = \frac{2(n_{\text{C}_2\text{H}_4} + n_{\text{C}_2\text{H}_6}) + 3(n_{\text{C}_3\text{H}_6} + n_{\text{C}_3\text{H}_8}) + 4(n_{\text{C}_4\text{H}_{10}})}{2(n_{\text{C}_2\text{H}_4} + n_{\text{C}_2\text{H}_6}) + 3(n_{\text{C}_3\text{H}_6} + n_{\text{C}_3\text{H}_8}) + 4(n_{\text{C}_4\text{H}_{10}}) + n_{\text{CO}} + n_{\text{CO}_2}} \times 100 \quad (2)$$

$$\% \text{CO}_x \text{ selectivity} = \frac{n_{\text{CO}} + n_{\text{CO}_2}}{2(n_{\text{C}_2\text{H}_4} + n_{\text{C}_2\text{H}_6}) + 3(n_{\text{C}_3\text{H}_6} + n_{\text{C}_3\text{H}_8}) + 4(n_{\text{C}_4\text{H}_{10}}) + n_{\text{CO}} + n_{\text{CO}_2}} \times 100 \quad (3)$$

$$\% \text{C}_{2+} \text{ yield} = \frac{\% \text{CH}_4 \text{ Conversion} \times \% \text{C}_{2+} \text{ Selectivity}}{100} \quad (4)$$

$$\frac{\text{Olefin}}{\text{Paraffin}} = \frac{2(n_{\text{C}_2\text{H}_4}) + 3(n_{\text{C}_3\text{H}_6})}{2(n_{\text{C}_2\text{H}_6}) + 3(n_{\text{C}_3\text{H}_8})} \quad (5)$$

$$r_{\text{C}_{2+}} = \frac{2(n_{\text{C}_2\text{H}_4} + n_{\text{C}_2\text{H}_6}) + 3(n_{\text{C}_3\text{H}_6} + n_{\text{C}_3\text{H}_8}) + 4(n_{\text{C}_4\text{H}_{10}})}{(\text{Total moles of MnTiO}_3 \text{ or (Mn + Ti) and Na}_2\text{WO}_4) \times h} \quad (6)$$

where n is the number of moles. The reported data is an average obtained from at least three separate catalytic tests. An example of carbon balance checks is shown in Supplementary Information Table S19.

Catalyst characterization. The morphology and metal dispersion of the catalysts were analyzed by field emission scanning electron microscopy with energy dispersive X-Ray spectroscopy (FE-SEM/EDS, FE-SEM: JEOL JSM7600F). Before the measurements, each catalyst was sputter-coated with platinum to increase the contrast for imaging.

The structural properties of each catalyst were examined by Fourier-transform infrared spectroscopy (FTIR; PerkinElmer Spectrum 400 FT-IR/FT-FIR). For each spectrum, 32 scans were collected over a spectral range of 400–4,000 cm^{-1} at a resolution of 4 cm^{-1} .

The crystal structure of each catalyst was analyzed by powder X-ray diffractometry (XRD; Bruker D8 Advance), using Cu-K α radiation at 45 kV and 40 mA with a step size of 0.02° and a step time of 0.5 s.

The surface area, pore size, and pore volume of each catalyst were measured by an N_2 -adsorption analyzer (3Flex Physisorption Micromeritics), following the Brunauer-Emmett-Teller (BET) method being conducted at –196 °C.

X-ray photoelectron spectroscopy (XPS; Kratos Axis Ultra DLD) was used to characterize the elements in each catalyst, namely sodium (Na 1 s), tungsten (W 4f), manganese (Mn 2p), titanium (Ti 2p), silicon (Si 2p), and oxygen (O 1 s). The binding energy of C 1 s (285.0 eV) was used as a standard for all other binding energies.

The particle size distribution of the samples was analyzed using high resolution–transmission electron microscopy with energy-dispersive X-ray spectroscopy (HR-TEM: JEM-2100). Each sample was suspended in ethanol

solvent, dropped on carbon film coated on Cu TEM grids, and dried in a chamber filled with N₂ at room temperature before the analysis.

Received: 21 September 2021; Accepted: 21 January 2022

Published online: 16 February 2022

References

- Holmen, A. Direct conversion of methane to fuels and chemicals. *Catal. Today* **142**, 2–8 (2009).
- IPCC. Climate Change 2013: The Physical Science Basis. (Geneva, Switzerland, 2013).
- United States Environmental Protection Agency. Overview of Greenhouse Gases, <https://www.epa.gov/ghgemissions/overview-greenhouse-gases#CH4-reference> (2019).
- Makaryan, B. I., Sedov, L. & Savchenko, V. Platinum group metal-catalysed carbonylation as the basis of alternative gas-to-liquids processes. *Johnson Matthey Technol. Rev.* **59**, 14–25 (2015).
- Sun, L., Wang, Y., Guan, N. & Li, L. Methane activation and utilization: Current status and future challenges. *Energy Technol.* **8**, 201900826 (2019).
- Karakaya, C., Zhu, H., Loebick, C., Weissman, J. G. & Kee, R. J. A detailed reaction mechanism for oxidative coupling of methane over Mn/Na₂WO₄/SiO₂ catalyst for non-isothermal conditions. *Catal. Today* **312**, 10–22 (2018).
- Zavyalova, U., Holena, M., Schlögl, R. & Baerns, M. Statistical analysis of past catalytic data on oxidative methane coupling for new insights into the composition of high-performance catalysts. *ChemCatChem* **3**, 1935–1947 (2011).
- Godini, H. R. *et al.* A multi-perspectives analysis of methane oxidative coupling process based on miniplant-scale experimental data. *Chem. Eng. Res. Des.* **151**, 56–69 (2019).
- Ji, S. *et al.* Surface WO₄ tetrahedron: the essence of the oxidative coupling of methane over M-W-Mn/SiO₂ catalysts. *J. Catal.* **220**, 47–56 (2003).
- Wang, J. *et al.* Comparative study on oxidation of methane to ethane and ethylene over Na₂WO₄-Mn/SiO₂ catalysts prepared by different methods. *J. Mol. Catal. A Chem.* **245**, 272–277 (2006).
- Chua, Y. T., Mohamed, A. R. & Bhatia, S. Oxidative coupling of methane for the production of ethylene over sodium-tungsten-manganese-supported-silica catalyst (Na-W-Mn/SiO₂). *Appl. Catal. A Gen.* **343**, 142–148 (2008).
- Malekzadeh, A., Dalai, A. K., Khodadadi, A. & Mortazavi, Y. Structural features of Na₂WO₄-MO_x/SiO₂ catalysts in oxidative coupling of methane reaction. *Catal. Commun.* **9**, 960–965 (2008).
- Yildiz, M. *et al.* Enhanced catalytic performance of Mn_xO_y-Na₂WO₄/SiO₂ for the oxidative coupling of methane using an ordered mesoporous silica support. *Chem. Commun.* **50**, 14440–14442 (2014).
- Yildiz, M. *et al.* Support material variation for the Mn_xO_y-Na₂WO₄/SiO₂ catalyst. *Catal. Today* **228**, 5–14 (2014).
- Yildiz, M. *et al.* Silica material variation for the Mn_xO_y-Na₂WO₄/SiO₂. *Appl. Catal. A Gen.* **525**, 168–179 (2016).
- Uzunoglu, C., Leba, A. & Yildirim, R. Oxidative coupling of methane over Mn-Na₂WO₄ catalyst supported by monolithic SiO₂. *Appl. Catal. A Gen.* **547**, 22–29 (2017).
- Hiyoshi, N. & Ikeda, T. Oxidative coupling of methane over alkali chloride-Mn-Na₂WO₄/SiO₂ catalysts: promoting effect of molten alkali chloride. *Fuel Process. Technol.* **133**, 29–34 (2015).
- Aseem, A., Jeba, G. G., Conato, M. T., Rimer, J. D. & Harold, M. P. Oxidative coupling of methane over mixed metal oxide catalysts: steady state multiplicity and catalyst durability. *Chem. Eng. J.* **331**, 132–143 (2018).
- Beck, B. *et al.* Oxidative coupling of methane: a complex surface/gas phase mechanism with strong impact on the reaction engineering. *Catal. Today* **228**, 212–218 (2014).
- Palermo, A., Vazquez, J. P. H., Tikhov, M. S. & Lambert, R. M. Critical influence of the amorphous silica-to-cristobalite phase transition on the performance of Mn/Na₂WO₄/SiO₂ catalysts for the oxidative coupling of methane. *J. Catal.* **177**, 259–266 (1998).
- Shahri, S. M. K. & Pour, A. N. Ce-promoted Mn/Na₂WO₄/SiO₂ catalyst for oxidative coupling of methane at atmospheric pressure. *J. Nat. Gas Chem.* **19**, 47–53 (2010).
- Reka, A. A., Pavlovski, B., Anovski, T., Bogoevski, S. & Boškovski, B. Phase transformations of amorphous SiO₂ in diatomite at temperature range of 1000–1200 °C. *Geol. Maced.* **29**, 87–92 (2015).
- Jiang, Z. C., Yu, C. J., Fang, X. P., Li, S. B. & Wang, H.-L. Oxide/support interaction and surface reconstruction in the sodium tungstate (Na₂WO₄)/silica system. *J. Phys. Chem. A* **97**, 12870–12875 (1993).
- Elkins, T. W. & Hagelin-Weaver, H. E. Characterization of Mn-Na₂WO₄/SiO₂ and Mn-Na₂WO₄/MgO catalysts for the oxidative coupling of methane. *Appl. Catal. A Gen.* **497**, 96–106 (2015).
- Werny, M. J., Wang, Y., Girgsdies, F., Schlögl, R. & Trunschke, A. Fluctuating storage of the active phase in a Mn-Na₂WO₄/SiO₂ catalyst for the oxidative coupling of methane. *Angew. Chem. Int. Ed.* **59**, 14921–14926 (2020).
- Sourav, S. *et al.* New Mechanistic and reaction pathway insights for oxidative coupling of methane (OCM) over supported Na₂WO₄/SiO₂ catalysts. *Angew. Chem. Int. Ed.* **60**, 21502–21511 (2021).
- Chukeaw, T. *et al.* Synthesis of value-added hydrocarbons via oxidative coupling of methane over MnTiO₃-Na₂WO₄/SBA-15 catalysts. *Process Saf. Environ. Prot.* **148**, 1110–1122 (2021).
- Ramalla, I., Gupta, R. K. & Bansal, K. Effect on superhydrophobic surfaces on electrical porcelain insulator, improved technique at polluted areas for longer life and reliability. *Int. J. Eng. Technol.* **4**, 509–519 (2015).
- Fleischer, V. *et al.* Investigation of the role of the Na₂WO₄/Mn/SiO₂ catalyst composition in the oxidative coupling of methane by chemical looping experiments. *J. Catal.* **360**, 102–117 (2018).
- Kiani, D., Sourav, S. & Wachs, I. E. Oxidative coupling of methane (OCM) by SiO₂-supported tungsten oxide catalysts promoted with Mn and Na. *ACS Catal.* **9**, 5912–5928 (2019).
- Malekzadeh, A. *et al.* Correlation of electrical properties and performance of OCM MO_x/Na₂WO₄/SiO₂ catalysts. *Catal. Commun.* **2**, 241–247 (2001).
- Sourav, S. *et al.* Resolving the types and origin of active oxygen species present in supported Mn-Na₂WO₄/SiO₂ catalysts for oxidative coupling of methane. *ACS Catal.* **11**, 10288–10293 (2021).
- Takanabe, K. *et al.* Integrated in situ characterization of a molten salt catalyst surface: evidence of sodium peroxide and hydroxyl radical formation. *Angew. Chem. Int. Ed.* **56**, 10403–10407 (2017).
- Wang, P., Zhao, G., Liu, Y. & Lu, Y. TiO₂-doped Mn₂O₃-Na₂WO₄/SiO₂ catalyst for oxidative coupling of methane: solution combustion synthesis and MnTiO₃-dependent low-temperature activity improvement. *Appl. Catal. A Gen.* **544**, 77–83 (2017).
- Sadjadi, S. *et al.* Feasibility study of the Mn-Na₂WO₄/SiO₂ catalytic system for the oxidative coupling of methane in a fluidized-bed reactor. *Catal. Sci. Technol.* **5**, 942–952 (2015).
- Mahmoodi, S., Ehsani, M. R. & Ghoreishi, S. M. Effect of promoter in the oxidative coupling of methane over synthesized Mn/SiO₂ nanocatalysts via incipient wetness impregnation. *J. Ind. Eng. Chem.* **16**, 923–928 (2010).
- Chukeaw, T., Sringam, S., Chareonpanich, M. & Seubsai, A. Screening of single and binary catalysts for oxidative coupling of methane to value-added chemicals. *Mol. Catal.* **470**, 40–47 (2019).

38. Kidamorn, P. *et al.* Synthesis of value-added chemicals via oxidative coupling of methanes over $\text{Na}_2\text{WO}_4\text{-TiO}_2\text{-MnO}_x/\text{SiO}_2$ catalysts with alkali or alkali earth oxide additives. *ACS Omega* **5**, 13612–13620 (2020).
39. Sringam, S., Kidamorn, P., Chukeaw, T., Chareonpanich, M. & Seubsai, A. Investigation of metal oxide additives onto $\text{Na}_2\text{WO}_4\text{-TiO}_2/\text{SiO}_2$ catalysts for oxidative coupling of methane to value-added chemicals. *Catal. Today* **358**, 263–269 (2020).
40. Gholipour, Z., Malekzadeh, A., Hatami, R., Mortazavi, Y. & Khodadadi, A. Oxidative coupling of methane over $(\text{Na}_2\text{WO}_4+\text{Mn}$ or $\text{Ce})/\text{SiO}_2$ catalysts: In situ measurement of electrical conductivity. *J. Nat. Gas Chem.* **19**, 35–42 (2010).
41. Wang, P., Zhao, G., Wang, Y. & Lu, Y. MnTiO_3 -driven low-temperature oxidative coupling of methane over TiO_2 -doped $\text{Mn}_2\text{O}_3\text{-Na}_2\text{WO}_4/\text{SiO}_2$ catalyst. *Sci. Adv.* **3**, e1603180. <https://doi.org/10.1126/sciadv.1603180> (2017).
42. Werny, M. J., Wang, Y., Girgsdies, F., Schlogl, R. & Trunschke, A. Fluctuating storage of the active phase in a $\text{Mn-Na}_2\text{WO}_4/\text{SiO}_2$ catalyst for the oxidative coupling of methane. *Angew. Chem. Int. Ed.* **59**, 14921–14926 (2020).
43. Aydin, Z. *et al.* Revisiting activity- and selectivity-enhancing effects of water in the oxidative coupling of methane over $\text{MnO}_x\text{-Na}_2\text{WO}_4/\text{SiO}_2$ and proving for other materials. *ACS Catal.* **10**, 8751–8764 (2020).
44. Ren, Y. *et al.* Membrane-based olefin/paraffin separations. *Adv. Sci.* **7**, 2001398. <https://doi.org/10.1002/adv.202001398> (2020).
45. Yunarti, R. T. *et al.* Oxidative coupling of methane using Mg/Ti -doped SiO_2 -supported $\text{Na}_2\text{WO}_4/\text{Mn}$ catalysts. *ACS Sustain. Chem. Eng.* **5**, 3667–3674 (2017).
46. Karlik, M. Lattice imaging in transmission electron microscopy. *Mater. Struct.* **8**, 3–16 (2001).
47. Gou, Q. *et al.* Facile synthesis of porous ternary $\text{MnTiO}_3/\text{TiO}_2/\text{C}$ composite with enhanced electrochemical performance as anode materials for lithium ion batteries. *Energy Technol.* **7**, 1800761. <https://doi.org/10.1002/ente.201800761> (2019).
48. Manukyan, K. V., Voskanyan, A. A., Rouvimov, S., Mukasyan, A. S. & Kharatyan, S. L. W and two-dimensional WO_3/W nanocrystals produced by controlled self-sustaining reduction of sodium tungstate. *J. Mater. Res.* **28**, 2611–2621 (2013).
49. Vaidya, S., Thaplyal, P. & Ganguli, A. K. Enhanced functionalization of $\text{Mn}_2\text{O}_3@/\text{SiO}_2$ core-shell nanostructures. *Nanoscale Res. Lett.* **6**, 169–174 (2011).
50. Trapp, M., Müller, M. M., Nazarpour, Z. & Kleebe, H.-J. Full reoxidation of CuMn_2O_4 spinel catalyst triggered by epitaxial Mn_3O_4 surface nanocrystals. *J. Am. Ceram. Soc.* **100**, 5327–5334 (2017).
51. Sen, M. Nanocomposite materials. *Nanotechnol. Environ.* <https://doi.org/10.5772/intechopen.93047> (2020).
52. Dedov, A. G. *et al.* Oxidative coupling of methane: Influence of the phase composition of silica-based catalysts. *Appl. Catal. A Gen.* **406**, 1–12 (2011).
53. Munasir, M., Triwikantoro, T., Zainuri, M. & Darminto, D. Synthesis of SiO_2 nanopowders containing quartz and cristobalite phases from silica sands. *Mater. Sci. Poland* **33**, 47–55 (2015).
54. Oh, T. & Choi, C. K. Comparison between SiOC thin film by plasma enhance chemical vapor deposition and SiO_2 thin film by fourier transform infrared spectroscopy. *J. Korean Phys. Soc.* **56**, 1150–1155 (2010).
55. Oh, T. Correlation between potential barrier and FTIR spectra in SiOC film with the C-O bond of sp^3 structure. *Bull. Korean Chem. Soc.* **30**, 467–470 (2009).
56. Tang, C. *et al.* Surface chemistry and reactivity of SiO_2 polymorphs: A comparative study on α -quartz and α -cristobalite. *Appl. Surf. Sci.* **355**, 1161–1167 (2015).
57. Ganesan, S., Ramasundari, P., Elangovan, A., Arivazhagan, G. & Vijayalakshmi, R. Synthesis and characterization of MnO_2 nanoparticles: Study of structural and optical properties. *Int. J. Sci. Res. Phys. Appl. Sci.* **5**, 5–8 (2017).
58. Rajakumar, G. *et al.* Fungus-mediated biosynthesis and characterization of TiO_2 nanoparticles and their activity against pathogenic bacteria. *Spectrochim. Acta. A Mol. Biomol. Spectrosc.* **91**, 23–29 (2012).
59. Al-Amin, M., Dey, S. C., Rashid, T. U., Ashaduzzaman, M. & Shamsuddin, S. M. Solar assisted photocatalytic degradation of reactive azo dyes in presence of anatase titanium dioxide. *Int. J. Latest Res. Eng. Technol.* **2**, 14–21 (2016).
60. Xu, J. *et al.* Developing reactive catalysts for low temperature oxidative coupling of methane: On the factors deciding the reaction performance of $\text{Ln}_2\text{Ce}_2\text{O}_7$ with different rare earth A sites. *Appl. Catal. A Gen.* **552**, 117–128 (2018).
61. Guittet, M. J., Crocombette, J. P. & Gautier-Soyer, M. Bonding and XPS chemical shifts in ZrSiO_4 versus SiO_2 and ZrO_2 : Charge transfer and electrostatic effects. *Phys. Rev. B* **63**, 125117 (2001).
62. Ingo, G. M., Riccucci, C., Bultrini, G., Dirè, S. & Chiozzini, G. Thermal and microchemical characterisation of Sol-Gel SiO_2 , TiO_2 and $x\text{SiO}_2\text{-(1-x)TiO}_2$ ceramic materials. *J. Therm. Anal. Calorim.* **66**, 37–46 (2001).
63. Zhang, B., Wang, P., Chen, Z., Gong, X. & Xu, M. XPS analysis pyrolytic char of cellulose with different crystallinity based on ionic liquid regeneration. *Appl. Mech. Mater.* **694**, 129–135 (2014).
64. Dupin, J. C., Gonbeau, D., Vinatier, P. & Levasseur, A. Systematic XPS studies of metal oxides, hydroxides and peroxides. *Phys. Chem. Chem. Phys.* **2**, 1319–1324 (2000).
65. Sharma, R. K., Rastogi, A. C. & Desu, S. B. Manganese oxide embedded polypyrrole nanocomposites for electrochemical supercapacitor. *Electrochim. Acta* **53**, 7690–7695 (2008).
66. Zhao, M., Ke, S., Wu, H., Xia, W. & Wan, H. Flower-like $\text{Sr-La}_2\text{O}_3$ microspheres with hierarchically porous structures for oxidative coupling of methane. *Ind. Eng. Chem. Res.* **58**, 22847–22856 (2019).
67. Sollier, B. M. *et al.* Synthesis and characterization of electrospun nanofibers of Sr-La-Ce oxides as catalysts for the oxidative coupling of methane. *Ind. Eng. Chem. Res.* **59**, 11419–11430 (2020).
68. Hayek, N. S., Lucas, N. S., Damouny, C. W. & Gazit, O. M. Critical surface parameters for the oxidative coupling of methane over the Mn-Na-W/SiO_2 catalyst. *ACS Appl. Mater. Interf.* **9**, 40404–40411 (2017).
69. Hayek, N. S., Khelif, G. J., Horani, F. & Gazit, O. M. Effect of reaction conditions on the oxidative coupling of methane over doped $\text{MnO}_x\text{-Na}_2\text{WO}_4/\text{SiO}_2$ catalyst. *J. Catal.* **376**, 25–31 (2019).
70. Enhessari, M., Parviz, A., Karamali, E. & Ozaee, K. Synthesis, characterisation and optical properties of MnTiO_3 nanopowders. *J. Exp. Nanosci.* **7**, 327–335 (2012).

Acknowledgements

This work was financially supported by the Office of the Ministry of Higher Education, Science, Research and Innovation, Thailand; the Thailand Science Research and Innovation through the Kasetsart University Re-inventing University Program 2021; the National Research Council of Thailand (NRCT5-RSA63002-11); and the Kasetsart University Research and Development Institute (KURDI), Thailand. Instrumental access was in part supported by the Austrian Science Fund (FWF) via grant SFB TACO (F81-P08).

Author contributions

W.T., T.C., S.S., and A.S. conducted the experiments and wrote the manuscript text. T.W. and M.C. consulted the results and provided funding. G.R. provided an access to use equipment and proofread the manuscript. A.S. managed the research. All authors reviewed the manuscript.

Competing interests

The authors declare no competing interests.

Additional information

Supplementary Information The online version contains supplementary material available at <https://doi.org/10.1038/s41598-022-06598-6>.

Correspondence and requests for materials should be addressed to A.S.

Reprints and permissions information is available at www.nature.com/reprints.

Publisher's note Springer Nature remains neutral with regard to jurisdictional claims in published maps and institutional affiliations.



Open Access This article is licensed under a Creative Commons Attribution 4.0 International License, which permits use, sharing, adaptation, distribution and reproduction in any medium or format, as long as you give appropriate credit to the original author(s) and the source, provide a link to the Creative Commons licence, and indicate if changes were made. The images or other third party material in this article are included in the article's Creative Commons licence, unless indicated otherwise in a credit line to the material. If material is not included in the article's Creative Commons licence and your intended use is not permitted by statutory regulation or exceeds the permitted use, you will need to obtain permission directly from the copyright holder. To view a copy of this licence, visit <http://creativecommons.org/licenses/by/4.0/>.

© The Author(s) 2022